Original Paper

Eletrônica de Potência
Open Journal of Power Electronics

Received June 11, 2026; Received in revised form August 17, 2026; Accepted August 31, 2026; Date of publication September 24, 2026.
The review of this paper was arranged by Associate Editor Filipe P. Scalcon and Editor-in-Chief Allan F. Cupertino.
Digital Object Identifier http://doi.org/10.18618/REP.e202629

Derivative-Free Decoupling Method for Asymmetric Six-Phase PMSMs Based on the Dual dq Reference Frame

Letícia D. Giovannini[1], **Arthur de C. B. Dias**[2], **Lenin M. F. Morais**[2], **Gabriel A. Fogli**[2,*]

[1]Aeronautics Institute of Technology, São José dos Campos, SP, Brazil.
[2]Universidade Federal de Minas Gerais, Graduate Program of Electrical Engineering, Belo Horizonte, MG, Brazil.

e-mail: leticia.giovannini.102256@ga.ita.br; arthurcarvalhobdias@ufmg.br; lenin@cpdee.ufmg.br; gabrielfogli@ufmg.br*.
*Corresponding author.

ABSTRACT This paper presents the modeling, control, and hardware-in-the-loop (HIL) evaluation of an asymmetric six-phase Permanent Magnet Synchronous Motor (6ϕ-PMSM) supplied by two three-phase Voltage Source Inverters (VSIs). The machine is modeled as two coupled three-phase subsystems using a dual dq representation. Based on this model, a cascade control structure composed of two parallel inner current loops and an outer speed loop is designed. A frequency-domain tuning methodology is also proposed, requiring only the selection of the inner closed-loop time constant and the desired phase margin of the outer loop, allowing all controller gains to be analytically obtained. To mitigate coupling effects between coordinates and subsystems and enable a single-input single-output (SISO) design approach, a decoupling strategy is proposed and comparatively analyzed. The proposed approach is directly derived from the state-space model and eliminates the need for state-variable derivatives, reducing sensitivity to switching noise and simplifying digital implementation. The control strategy is verified through HIL test bench, in which the plant is implemented in the HIL platform while the control algorithm is executed in a digital signal processor. Experimental results demonstrate accurate dynamic behavior, fast current response, reduced coupling effects, and low current harmonic distortion under different operating conditions.

KEYWORDS Six-phase PMSM, Machine drives, Control applied to power electronics, Decoupling Method.

I. INTRODUCTION

The increasing demand for electric vehicles (EVs), driven by advances in battery technology and growing environmental concerns, has intensified the research interest in high-efficiency electric drive systems [1]–[3]. In this context, the Permanent Magnet Synchronous Motor (PMSM) has become one of the most widely adopted electrical machines in EV applications due to its high efficiency, high power density, and absence of mechanical commutators and brushes [4]. To further improve the performance and competitiveness of EVs, machines with more than three phases, commonly referred to as multiphase machines, have attracted considerable attention in recent years. Compared with conventional three-phase machines, multiphase motors offer several advantages, including higher efficiency, reduced harmonic distortion, lower torque ripple, enhanced reliability, and improved fault-tolerant capability. [5]. As a result, asymmetric six-phase PMSMs (6ϕ-PMSMs) have emerged as an attractive solution for high-performance drive applications.

The 6ϕ-PMSM has been investigated in several applications due to its modular structure, fault-tolerant capability, and improved power distribution. In renewable energy systems, it has been proposed for microgrid and flywheel energy storage applications [6]. Moreover, the use of 6ϕ-PMSMs has been widely investigated in electric vehicles [7] and aircraft propulsion systems [8], as well as in hybrid energy storage systems integrated with electric drives [9].

Different control and modeling approaches for 6ϕ-PMSMs have also been reported in the literature. Current control strategies based on Vector Space Decomposition (VSD) and modular vector control have been investigated in [10], [11], while improved decoupling techniques have been proposed to mitigate steady-state imbalance and cross-coupling effects between subspaces [12]. Furthermore, several studies have focused on improving the dynamic performance and robustness of multiphase drives through harmonic suppression techniques, and observer-based approaches [13]–[18].

Despite these advances, the increased system complexity associated with multiphase machines still imposes challenges regarding mathematical modeling, coordinate decoupling, and practical digital implementation. Although several control strategies for multiphase PMSMs have been reported, important challenges still remain regarding the development of simplified and explicit mathematical models suitable for control-oriented applications. In particular, the coupling effects between subspaces, in dual dq approach, increase the complexity of the control design and require additional compensation terms to enable independent current regulation. In this context, conventional decoupling approaches typically rely on voltage-equation formulations that contain derivatives of the state-variables. To facilitate their practical implementation, the coupling between subsystems is often neglected [19]. Although this approximation ensures zero steady-state error, it compromises the controller's dynamic performance, since the system remains subject to interactions among multiple inputs. Furthermore, derivative terms are generally undesirable in power electronics applications because they increase sensitivity to switching noise, measurement ripple, and numerical inaccuracies. Consequently, the development of computationally efficient decoupling strategies that provide improved noise immunity while preserving dynamic performance remains an important research topic in multiphase drive systems.

Another decoupling method is presented in [20], however this method is presented for VSD-based control. Despite the effectiveness of VSD, the original VSD-based vector control scheme [21] suffers from certain limitations, including the inability to guarantee balanced current sharing among the winding sets. In [22] is mentioned that the dual dq approach causes complex cross coupling between the two pairs of dq stator voltage equations that is very difficult to eliminate in PMSM drives. As a consequence, good dynamic performance is hard to achieve using such vector control schemes.

Existing decoupling strategies for 6ϕ-PMSMs can be classified into two categories. The first comprises methods derived directly from the machine voltage-equations, in which the compensation terms require state-variable derivatives, increasing sensitivity to switching ripple, measurement noise, and numerical inaccuracies during digital implementation. The second category includes approaches based on VSD, which rely on a different modeling and control framework than the dual dq representation, adopted in this work. In contrast, the proposed strategy is directly derived from the state-space representation of the dual dq model, preserving the original control architecture while eliminating the need for current derivative calculations.

To address these challenges, this work proposes a decoupling strategy directly derived from the state-space representation and eliminates the need for derivative terms for the asymmetric 6ϕ-PMSM controlled by dual dq approach. Besides that, the main contributions of this work are summarized as follows:

1) A control-oriented state-space model of the asymmetric 6ϕ-PMSM, including the relevant coupling dynamics between subsystems.
2) A derivative-free decoupling strategy derived from the state-space representation, reducing sensitivity to switching noise and simplifying real-time digital implementation.
3) A frequency-domain tuning methodology based solely on the selection of the inner current-loop time constant and the desired phase margin, allowing all controller gains to be analytically determined.
4) A comparative analysis about the proposed decoupling approach under hardware-in-the-loop operation (HIL) with DSP-based control implementation.

This paper presents the modeling, control design, and performance evaluation of an asymmetric 6ϕ-PMSM supplied by two three-phase VSIs. A control-oriented state-space representation of the machine is developed, allowing the investigation of a novel decoupling strategy for current control applications. In addition, a cascaded control architecture composed of parallel inner current loops and an outer speed loop is designed and implemented. To evaluate the proposed approaches, the system is implemented in a HIL platform, while the control algorithm is executed in a DSP-based environment. The obtained results are used to comparatively analyze the decoupling strategy in terms of dynamic response, coupling mitigation, disturbance rejection, and implementation suitability for digitally controlled power electronics systems.

II. SYSTEM MODELING

The asymmetric round rotor 6ϕ-PMSM round rotor considered in this work consists of two three-phase stator windings spatially shifted by $30°$ electrical degrees. The machine is supplied by two independent three-phase Voltage Source Inverters (VSIs) sharing a common DC-link, as illustrated in Figure 1.

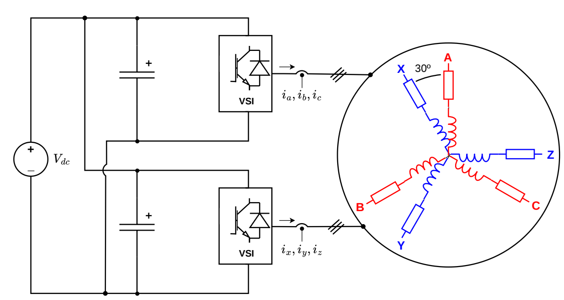

FIGURE 1. Asymetric 6ϕ-PMSM driven by two three-phase VSIs.

To achieve high dynamic performance and accurate current regulation, field-oriented control (FOC) is adopted. The control strategy is implemented in the synchronous dq reference frame, enabling the use of PI-based current controllers. In addition, decoupling terms are incorporated into the control loops to mitigate the coupling effects between coordinates and between the two three-phase subsystems.

By applying the Park transform to the two three-phase subsystems, the electrical dynamics of the 6ϕ-PMSM can be expressed in dq reference frame. The resulting model includes the stator resistance terms, self-inductance components, and mutual coupling terms between the two subsystems. It is worth noting that the $30°$ electrical displacement between the two stator winding sets is incorporated into the dual dq transformation. The first three-phase subsystem is transformed using the electrical angle θ, whereas the second subsystem is transformed using $\theta + \pi/6$. Consequently, the spatial displacement is inherently included in the resulting mathematical model.

Figure 2 depicts the equivalent circuit of the 6ϕ-PMSM considering the dual dq reference frame. Accordingly, the machine electrical model is described by:

$$\begin{bmatrix} v_{d1} \\ v_{q1} \\ v_{d2} \\ v_{q2} \end{bmatrix} = \begin{bmatrix} R_s & -\omega L_q & 0 & -\omega M_q \\ \omega L_d & R_s & \omega M_d & 0 \\ 0 & -\omega M_q & R_s & -\omega L_q \\ \omega M_d & 0 & \omega L_d & R_s \end{bmatrix} \begin{bmatrix} i_{d1} \\ i_{q1} \\ i_{d2} \\ i_{q2} \end{bmatrix} + \begin{bmatrix} L_d & 0 & M_d & 0 \\ 0 & L_q & 0 & M_q \\ M_d & 0 & L_d & 0 \\ 0 & M_q & 0 & L_q \end{bmatrix} \begin{bmatrix} \dot{i}_{d1} \\ \dot{i}_{q1} \\ \dot{i}_{d2} \\ \dot{i}_{q2} \end{bmatrix} + \begin{bmatrix} 0 \\ \omega \\ 0 \\ \omega \end{bmatrix} \lambda_m, \quad (1)$$

where L represents the self-inductance, M is the mutual inductance between the subsystems, R_s is the stator resistance, ω is the electrical angular speed, i and v denote the current and voltage variables in the dq frame, respectively, and λ_m is the permanent magnet flux linkage. In this study, self and mutual inductance in d and q coordinates are considered equal ($L_{dq} = L_d = L_q$ and $M_{dq} = M_d = M_q$).

For control design purposes, the machine model is reformulated in a state-space representation. The state-variables are defined as the dq currents of both three-phase subsystems, while the control inputs correspond to the voltages generated by the VSIs. Accordingly, the state-space formulation can be expressed as:

$$\begin{bmatrix} \dot{i}_{d1} \\ \dot{i}_{q1} \\ \dot{i}_{d2} \\ \dot{i}_{q2} \end{bmatrix} = \mathbf{E}^{-1} \begin{bmatrix} -R_s & \omega L_{dq} & 0 & \omega M_{dq} \\ -\omega L_{dq} & -R_s & -\omega M_{dq} & 0 \\ 0 & -\omega M_{dq} & -R_s & \omega L_{dq} \\ -\omega M_{dq} & 0 & -\omega L_{dq} & -R_s \end{bmatrix} \begin{bmatrix} i_{d1} \\ i_{q1} \\ i_{d2} \\ i_{q2} \end{bmatrix} + \mathbf{E}^{-1} \begin{bmatrix} v_{d1} \\ v_{q1} \\ v_{d2} \\ v_{q2} \end{bmatrix} + \mathbf{E}^{-1} \begin{bmatrix} 0 \\ \omega \\ 0 \\ -\omega \end{bmatrix} \lambda_m, \quad (2)$$

$$\mathbf{E} = \begin{bmatrix} L_{dq} & 0 & M_{dq} & 0 \\ 0 & L_{dq} & 0 & M_{dq} \\ M_{dq} & 0 & L_{dq} & 0 \\ 0 & M_{dq} & 0 & L_{dq} \end{bmatrix}. \quad (3)$$

Matrix $\mathbf{E}$ contains the self- and mutual-inductance terms associated with the coupling between the two three-phase subsystems. Thus, applying the necessary manipulations, the state-space representation can be rewritten as:

$$\begin{aligned} \begin{bmatrix} \dot{i}_{d1} \\ \dot{i}_{q1} \\ \dot{i}_{d2} \\ \dot{i}_{q2} \end{bmatrix} &= \begin{bmatrix} -\sigma_1 R_s & \omega & \sigma_2 R_s & 0 \\ -\omega & -\sigma_1 R_s & 0 & \sigma_2 R_s \\ \sigma_2 R_s & 0 & -\sigma_1 R_s & \omega \\ 0 & \sigma_2 R_s & -\omega & -\sigma_1 R_s \end{bmatrix} \begin{bmatrix} i_{d1} \\ i_{q1} \\ i_{d2} \\ i_{q2} \end{bmatrix} \\ &+ \begin{bmatrix} \sigma_1 & 0 & -\sigma_2 & 0 \\ 0 & \sigma_1 & 0 & -\sigma_2 \\ -\sigma_2 & 0 & \sigma_1 & 0 \\ 0 & -\sigma_2 & 0 & \sigma_1 \end{bmatrix} \begin{bmatrix} v_{d1} \\ v_{q1} \\ v_{d2} \\ v_{q2} \end{bmatrix} \\ &+ \begin{bmatrix} 0 \\ \omega(\sigma_2 - \sigma_1) \\ 0 \\ \omega(\sigma_2 - \sigma_1) \end{bmatrix} \lambda_m, \\ \mathbf{y} &= \mathbf{I}_4 \begin{bmatrix} i_{d1} & i_{q1} & i_{d2} & i_{q2} \end{bmatrix}^T, \\ \sigma_1 &= \frac{L_{dq}}{L_{dq}^2 - M_{dq}^2}, \qquad \sigma_2 = \frac{M_{dq}}{L_{dq}^2 - M_{dq}^2}. \end{aligned} \quad (4)$$

The coefficients σ_1 and σ_2 define the relationship between the self- and mutual-inductance terms and explicitly characterize the coupling dynamics between the subsystems. This representation is particularly suitable for control-oriented analysis, since it provides a clear separation between the system dynamics, control inputs, and coupling terms.

A. Decoupling Strategies

The electrical dynamics of the 6ϕ-PMSM present cross-coupling terms between coordinates and subsystems. As a consequence, each current component is influenced by multiple state-variables and control inputs, which increases the complexity of the controller design and degrades the independent regulation of the dq currents.

To mitigate these coupling effects and allow the current control loops to be designed as equivalent single-input single-output (SISO) system, decoupling strategies are incorporated into the control structure. In this work, two different decoupling approaches are investigated and comparatively analyzed.

The first approach is directly derived from the voltage-equations of the machine model, as shown in [19]. The second approach, proposed in this work, is obtained from the explicit state-space representation of the system. Due to the different arrangement of the dynamic and input matrices in each formulation, the resulting decoupling terms are structurally different and lead to distinct implementation characteristics and dynamic responses.

Unlike the conventional decoupling strategy, the proposed state-space-based approach does not require the computation of current derivatives. This characteristic is particularly advantageous for digitally controlled power electronics systems, since derivative operations tend to amplify switching noise and measurement ripple. In addition, the proposed formulation provides a more direct implementation of the decoupling terms, improving the compatibility with real-time DSP-based control platforms.

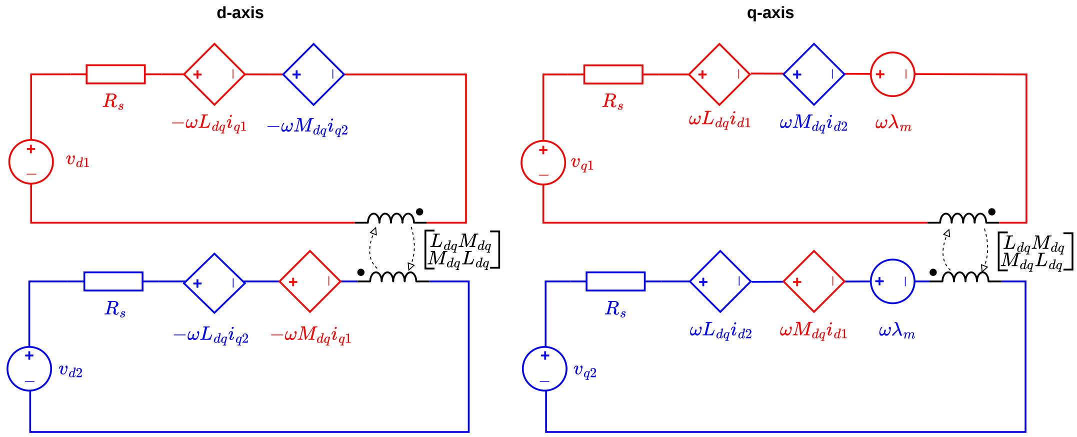

FIGURE 2. Equivalent circuit of the 6ϕ PMSM in dual dq reference frame.

By directly compensating the coupling terms present in the voltage equations of the machine model (1), the decoupling terms are described by:

$$v_{d1,\mathrm{dec1}} = -\omega L_{dq} i_{q1} - \omega M_{dq} i_{q2} + M_{dq} \frac{di_{d2}}{dt}, \quad (5)$$

$$v_{q1,\mathrm{dec1}} = \omega L_{dq} i_{d1} + \omega M_{dq} i_{d2} + M_{dq} \frac{di_{q2}}{dt} + \omega \lambda_m, \quad (6)$$

$$v_{d2,\mathrm{dec1}} = -\omega L_{dq} i_{q2} - \omega M_{dq} i_{q1} + M_{dq} \frac{di_{d1}}{dt}, \quad (7)$$

$$v_{q2,\mathrm{dec1}} = \omega L_{dq} i_{d2} + \omega M_{dq} i_{d1} + M_{dq} \frac{di_{q1}}{dt} + \omega \lambda_m. \quad (8)$$

Alternatively, by using the explicit state-space representation given in (4), the decoupling terms can be reformulated as:

$$v_{d1,\mathrm{dec2}} = -\frac{L_{dq}^2 - M_{dq}^2}{L_{dq}} \omega i_{q1} - \frac{M_{dq}}{L_{dq}} R_s i_{d2} + \frac{M_{dq}}{L_{dq}} v_{d2}, \quad (9)$$

$$\begin{aligned} v_{q1,\mathrm{dec2}} = {} & \frac{L_{dq}^2 - M_{dq}^2}{L_{dq}} \omega i_{d1} - \frac{M_{dq}}{L_{dq}} R_s i_{q2} + \frac{M_{dq}}{L_{dq}} v_{q2} \\ & - \frac{M_{dq} - L_{dq}}{L_{dq}^2 - M_{dq}^2} \omega \lambda_m, \end{aligned} \quad (10)$$

$$v_{d2,\mathrm{dec2}} = -\frac{L_{dq}^2 - M_{dq}^2}{L_{dq}} \omega i_{q2} - \frac{M_{dq}}{L_{dq}} R_s i_{d1} + \frac{M_{dq}}{L_{dq}} v_{d1}, \quad (11)$$

$$\begin{aligned} v_{q2,\mathrm{dec2}} = {} & \frac{L_{dq}^2 - M_{dq}^2}{L_{dq}} \omega i_{d2} - \frac{M_{dq}}{L_{dq}} R_s i_{q1} + \frac{M_{dq}}{L_{dq}} v_{q1} \\ & - \frac{M_{dq} - L_{dq}}{L_{dq}^2 - M_{dq}^2} \omega \lambda_m. \end{aligned} \quad (12)$$

It can be observed that the proposed decoupling strategy replaces the derivative-dependent compensation terms by algebraic terms directly related to the system states and inputs. This characteristic simplifies the digital implementation and avoids the amplification of switching ripple and measurement noise typically associated with derivative operations in switched power electronic systems.

The proposed derivative-free decoupling methodology is derived directly from the state-space representation and is therefore not restricted to the particular case $L_d = L_q = L_{dq}$ and $M_d = M_q = M_{dq}$, considered in this work. For salient-pole machines, $L_d \neq L_q$ and $M_d \neq M_q$, the state-space model in (4) and the resulting decoupling terms would naturally differ according to the machine parameters. Nevertheless, the proposed state-space-based derivation procedure remains applicable.

B. Control-Oriented SISO Representation

Assuming an effective compensation of the coupling terms through the adopted decoupling strategy, the dq current dynamics of the asymmetric 6ϕ-PMSM can be approximated as independent first-order SISO systems. Under this assumption, the simplified current dynamics can be obtained from the state-space representation in (4).

By applying the Laplace transform, the equivalent transfer functions relating the dq currents and voltages for both subsystems are given by:

$$G_i(s) = \frac{I_{dq,1}}{V_{dq,1}} = \frac{I_{dq,2}}{V_{dq,2}} = \frac{1}{s\left(\frac{L_{dq}^2 - M_{dq}^2}{L_{dq}}\right) + R_s}, \quad (13)$$

$$G_i(s) = \frac{1}{sL_f + R_s}. \quad (14)$$

where $L_f = (L_{dq}^2 - M_{dq}^2)/L_{dq}$ represents the equivalent inductance associated with the decoupled current dynamics.

III. CURRENT CONTROLLER LOOP DESIGN

The control system is organized in a cascaded architecture composed of two parallel inner current control loops and an outer speed control loop, as illustrated in Figure 3. Each inner loop regulates the dq currents of one three-phase subsystem, while the outer loop is responsible for the rotor speed regulation.

Since both three-phase subsystems present identical electrical dynamics and equally contribute to torque production, the q-axis current reference generated by the speed controller is equally distributed between the two subsystems, resulting in $i_{q1}^* = i_{q2}^* = 0.5\ i_q^*$. The d-axis current references are set to zero, resulting in $i_{d1}^* = i_{d2}^* = 0$, which corresponds to the MTPA operating condition for the adopted machine, with $L_d = L_q$ [23].

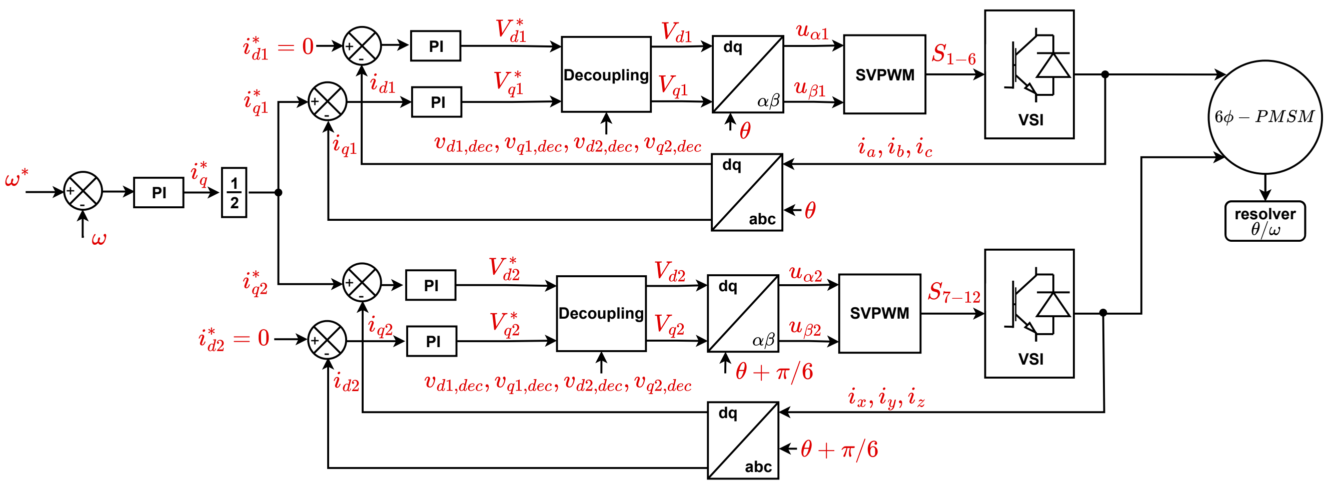

FIGURE 3. Block diagram of the control system.

Since both three-phase subsystems exhibit identical electrical dynamics, the current controllers are designed using the same procedure and parameters. The current regulation is performed using PI controllers due to the constant behavior of the reference signals. For this work, the controller parameters are selected using pole-zero cancellation, placing the controller zero at the same location as the plant pole, i.e., at R_s/L_f. Under this condition, the open-loop transfer function becomes:

$$H_{i,ol}(s) = \frac{sk_p + k_i}{s}\frac{1}{sL_f + R_s} = \frac{k_p}{sL_f}, \tag{15}$$

with,

$$k_p = \frac{L_f}{\tau_i}, \tag{16}$$

$$k_i = \frac{R_s}{\tau_i}, \tag{17}$$

where τ_i represents the desired closed-loop current time constant. Accordingly, the closed-loop transfer function can be expressed as:

$$H_{i,cl}(s) = \frac{i_{dq,1}}{i_{dq,1}^*} = \frac{i_{dq,2}}{i_{dq,2}^*} = \frac{k_p}{L_f(s + \frac{k_p}{L_f})} = \frac{1}{\tau_i s + 1}. \tag{18}$$

The resulting closed-loop current dynamics exhibit a first-order response characterized by the time constant τ_i, providing a fast transient response without overshoot during current reference variations. The value of τ_i is selected considering the switching frequency and the desired current control bandwidth, typically ranging from $0.5\ ms$ to $5\ ms$ for VSIs operating at switching frequencies of several kilohertz.

Different approaches may be employed for the current controller design, but in this work, pole-zero cancellation is adopted because it yields a first-order closed-loop current response. This characteristic is subsequently exploited in the outer-loop design and serves as a reference for evaluating the effectiveness of the proposed decoupling method.

The current controller design assumes that the coupling effects between coordinates and subsystems are effectively compensated, allowing each dq current loop to be treated as an equivalent SISO system. Therefore, the decoupling terms derived in Section II-A are incorporated into the control structure to mitigate the cross-coupling dynamics.

IV. SPEED CONTROLLER LOOP DESIGN

The outer control loop is responsible for regulating the rotor speed and generating the q-axis current reference for the inner current controllers, as illustrated in Figure 4. Since the influence of the viscous friction coefficient is several orders of magnitude smaller than the electromagnetic torque, B is assumed to be negligible in this work. Under this assumption, the simplified mechanical dynamics can be expressed as:

$$G_\omega(s) \approx \frac{k_t}{sJ}, \tag{19}$$

where J is the moment of inertia; $k_t = 3N\lambda_m$ is the torque constant; N is the number of pair of poles and λ_m is the magnetic flux.

For the outer speed loop, the closed-loop current dynamics described by (18) are explicitly considered in the controller design. Since the current loop bandwidth is significantly higher than the mechanical bandwidth, the speed controller $C_\omega(s)$ can be designed based on the cascade connection between the mechanical dynamics and the inner current closed-loop response.

A PI controller is adopted for the speed regulation loop in order to eliminate steady-state speed error. Thus, the speed controller is defined as:

$$C_\omega(s) = k_\omega\left(\frac{s+\lambda}{s}\right), \tag{20}$$

and the forward path depicted in Figure 4 is described as,

$$H_{\omega,ol}(s) = C_\omega(s)H_{i,cl}(s)G_\omega(s). \tag{21}$$

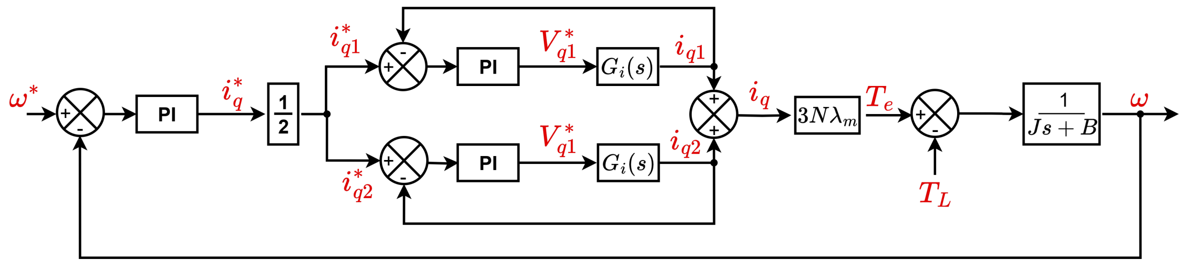

FIGURE 4. Speed control loop.

Substituting (18), (19), and (20), into (21) yields,

$$H_{\omega,ol}(s) = \left(k_\omega \frac{s+\lambda}{s}\right)\left(\frac{1}{s\tau_i+1}\right)\left(\frac{k_t}{sJ}\right). \tag{22}$$

Since the open-loop transfer function contains two integrators and one additional real pole associated with the inner current dynamics, the controller's zero is selected such that $\lambda < \tau_i^{-1}$. Under this condition, the maximum phase contribution introduced by the controller occurs at the frequency [24]:

$$\omega_{PM} = \sqrt{\lambda\tau_i^{-1}}, \tag{23}$$

$$PM = \sin^{-1}\left(\frac{1-\tau_i\lambda}{1+\tau_i\lambda}\right). \tag{24}$$

By selecting the crossover frequency of $H_{\omega,ol}(s)$ equal to ω_{PM}, the maximum phase contribution of the controller directly establishes the phase margin (PM) of the speed loop. Therefore, the proportional gain k_ω is selected such that, $|H_{\omega,ol}(j\omega_{PM})| = 1$, which results in:

$$k_\omega = \frac{J\omega_{PM}}{k_t}. \tag{25}$$

This design methodology allows the speed loop bandwidth and phase margin to be explicitly adjusted while preserving the bandwidth separation between the mechanical and electrical dynamics.

V. HIL PERFORMANCE EVALUATION

For this study, the 6ϕ-PMSM parameters are based on [25] and are listed in Table 1.

TABLE 1. 6ϕ**-PMSM parameters.**

Parameter	Value
Rated power P_n	1 kW
Rated current I_n	13.5 A
Number of pole pairs N	5
Magnetic flux λ_m	0.0135 Vs/rad
Rated speed n_n	3000 rpm
Rated voltage V_n	48 V
Winding resistance R_s	0.12 Ω
Moment of inertia	0.001 kgm^2
d-axis inductance L_d	0.5 mH
d-axis mutual inductance M_d	0.2 mH
q-axis inductance L_q	0.5 mH
q-axis mutual inductance M_q	0.2 mH

Furthermore, the proposed tuning procedure is based solely on the selection of two design parameters, τ_i and PM, from which all controller gains are analytically determined. Accordingly, by selecting $\tau_i = 0.5$ ms and $PM = 53°$, the resulting controller gains are listed in Table 2, and, Figure 5 depicts $H_{\omega,ol}(s)$ frequency response. By substituting the parameters listed in Table 2 into (22) and deriving the corresponding closed-loop transfer function of the speed control loop, a closed-loop bandwidth of about 174 Hz is obtained.

TABLE 2. Controller Gains.

Current Controllers		Speed Controller	
Parameter	**Value**	**Parameter**	**Value**
k_p	0.8	k_ω	3.3
k_i	240	λ	223.9

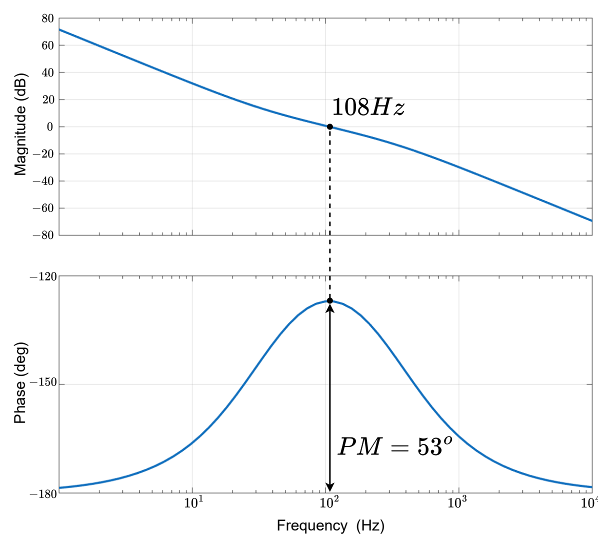

FIGURE 5. Frequency response of $H_{\omega,ol}(s)$, highlighting a PM of $53°$ at $108\ Hz$.

During the study, a load coupled to the motor shaft is considered, modeled as a fan whose torque presents a quadratic relationship,

$$T_L = sign(\omega_m)\left(\frac{T_n}{\omega_n}\right)\omega_m^2, \tag{26}$$

and,

$$\frac{T_n}{\omega_n} = \frac{3N\lambda_m I_n}{\omega_n^2} = 27.7\mu, \quad (27)$$

where ω_n is the nominal speed in rad/s; ω_m is the instantaneous mechanical speed in rad/s.

A. Test Bench Description

To validate the proposed control strategies and comparatively evaluate the decoupling approach, the drive system is implemented in a real-time HIL platform. In the adopted configuration, the asymmetric 6ϕ-PMSM and the VSI are implemented in the HIL environment, as shown in Figure 6. The HIL plant is executed with a fixed simulation time step of 5×10^{-6} s. The control loops and PWM generation routines are executed in the LAUNCHXL-F28379D DSP board provided by Texas Instruments.

The experimental setup is shown in Figure 7. The measured signals are properly scaled based on the DSP analog-to-digital converter (ADC) input range, which is $0\ V$ to $3\ V$. Accordingly, the current measurements are normalized considering a maximum current of $20\ A$, while the DC-link voltage is normalized to a base value of $200\ V$. The rotor speed signal is scaled according to a maximum operating speed of $300\ rad/s$, about $2865\ rpm$. The sampling and switching frequencies are both $20\ kHz$, with a dead time of 0.1×10^{-6} s considered in the PWM generation. The controller is discretized using the Trapezoidal method.

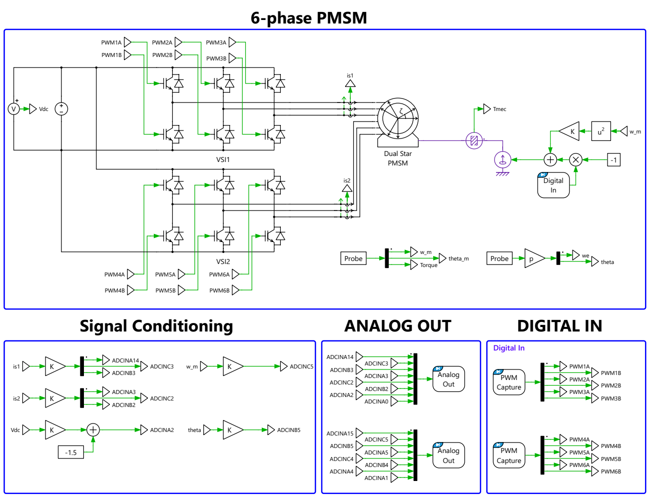

FIGURE 6. System implementation in PLECS environment.

B. Current Controller

Figure 8 presents the dual dq current responses for the three conditions. In all cases, simultaneous step references of $6\ A$ are applied to (i_{q1}^*) and (i_{q2}^*), while the d-axis current references remain at zero. Table 3 summarizes the settling time and overshoot measured for the three evaluated current control strategies, providing a quantitative comparison of their transient performance.

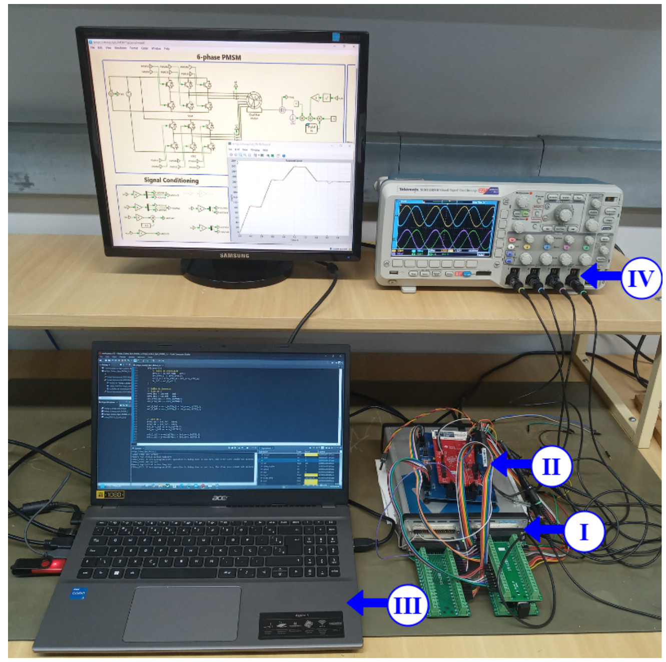

FIGURE 7. Test bench: i) RT-BOX CE HIL system from PLEXIM, (ii) LaunchXL-F28379D DSP board from Texas Instruments, (iii) computer, and (iv) oscilloscope.

Without decoupling, shown in Figure 8 (a), the coupling effects between coordinates and between the two three-phase subsystems significantly affect the current regulation dynamics. As a consequence, the current responses exhibit slower transient behavior, increased settling time of about $12\ ms$, instead of $2\ ms$ ($4 \times \tau_i$) chosen in the current controller design section. Under this condition, the current controllers are unable to reproduce the designed first-order dynamics due to the influence of uncompensated cross-coupling terms in the machine model. An overshoot of about 7% is observed under this condition.

TABLE 3. Transient response metrics for the evaluated decoupling methods.

Decoupling method	Settling time	Overshoot
Without decoupling (Figure 8 (a))	$12\ ms$	7%
Derivative-based (Figure 8 (b))	$2\ ms$	0%
Proposed Derivative-free (Figure 8 (c))	$2\ ms$	0%

Figure 8 (b) presents the response obtained using the conventional derivative-based decoupling strategy. In this case, the compensation of the coupling terms considerably improves the transient dynamics, reducing the settling time and increasing the bandwidth of the current loops. However, despite the improved dynamic response, the current signals exhibit pronounced high-frequency oscillations and increased ripple levels. As expected, this behavior is associated with the derivative operations required by the conventional decoupling formulation, since derivative terms inherently amplify switching ripple, quantization effects, and measurement

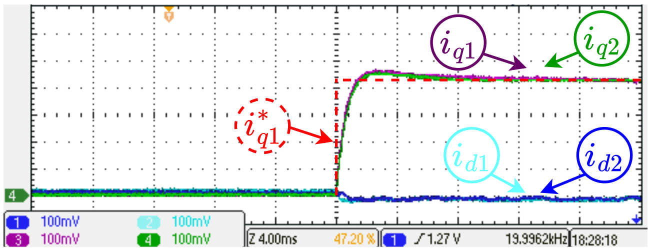

(a)

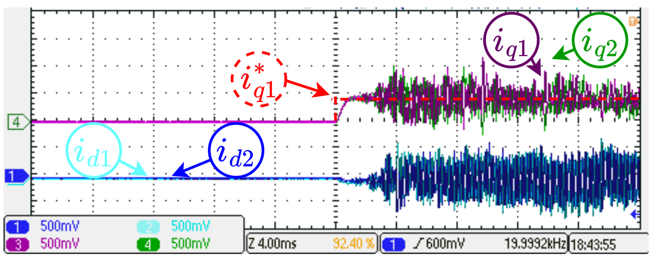

(b)

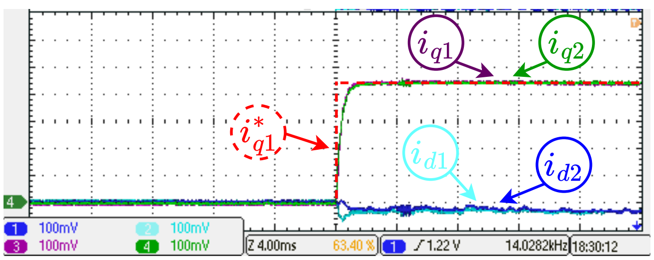

(c)

FIGURE 8. Comparison of dq current responses under a $6\ A$ q-axis current step for different decoupling strategies: (a) without decoupling ($1.33\ A/div$ for all channels), (b) conventional derivative-based decoupling ($6.66\ A/div$ for all channels), and (c) proposed derivative-free decoupling ($1.33\ A/div$ for all channels).

noise in digitally controlled power electronics systems. As a result, although the coupling compensation becomes effective from a dynamic perspective, the implementation presents reduced signal quality under real-time DSP execution.

The response obtained using the proposed derivative-free decoupling strategy is shown in Figure 8 (c). In contrast to the conventional implementation, the proposed approach achieves fast current regulation while maintaining smooth and low-noise current waveforms. Since the decoupling terms do not require state-variable derivatives, the transient response matches the designed first-order current dynamics established during the controller tuning procedure, presenting an approximate settling time of $2\ ms$, consistent with the selected $\tau_i = 0.5\ ms$.

The comparative results demonstrate that the proposed derivative-free strategy preserves the dynamic advantages of the decoupling action while significantly improving implementation suitability for digitally controlled systems. Therefore, the proposed method constitutes an effective alternative for high-performance multiphase drive applications requiring fast current regulation and reduced sensitivity to measurement noise.

C. Speed Controller

The performance of the cascaded control architecture is evaluated through transient speed response tests under different operating conditions. Figure 9 presents the rotor speed response and the corresponding dq current dynamics for a step variation in the speed reference of $200\ rpm$ using the proposed derivative-free decoupling strategy. As observed, the rotor speed accurately tracks the imposed reference while maintaining stable current regulation during the transient interval. An overshoot of $25\ \%$ in the mechanical speed is achieved in accordance with the speed controller design.

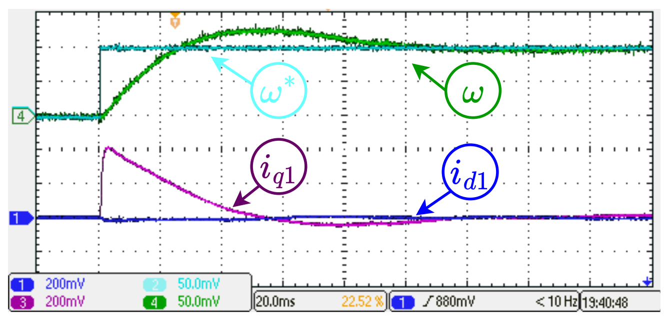

FIGURE 9. Rotor speed and dq current responses to a $200\ rpm$ speed reference step using the proposed derivative-free decoupling method (Channel 4: $100\ rpm/div$; Channels 1 and 3: $2.66\ A/div$; Channel 2: $50\ rpm/div$).

To further evaluate the controller performance under representative drive operating conditions, a speed profile including acceleration, soft-start, braking, and load disturbance events is implemented, as summarized in Table 4. The corresponding responses are shown in Figure 10.

TABLE 4. Events description. All rise and fall times are of $0.2\ s$.

Event	Description
A	Acceleration in ramp from 0 to 1000 rpm
B	Acceleration in ramp from 1000 to 2000 rpm
C	Acceleration in ramp from 2000 to 2500 rpm
D	Deceleration in ramp from 2000 to 2500 rpm
E	Step load of 1 $N.m$

During the acceleration and braking intervals, the controller maintains smooth speed transitions and stable current regulation, without presenting instability or excessive transient oscillations. Furthermore, when the load disturbance is applied, the controller rapidly compensates the torque variation and restores the rotor speed to its reference value with negligible steady-state error. These results demonstrate the effectiveness of the proposed tuning methodology and confirm the suitability of the control structure for high-performance multiphase drive applications.

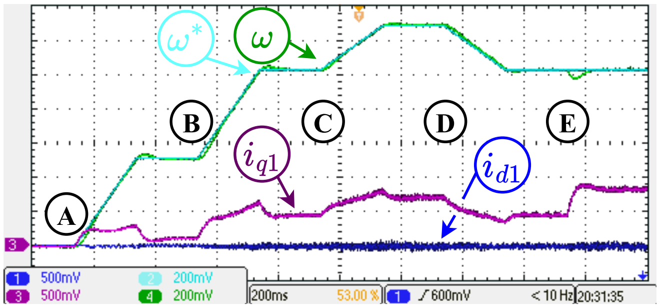

FIGURE 10. Rotor speed and dq current responses during the driving profile defined in Table 4 using the proposed derivative-free decoupling strategy (Channels 2 and 4: $400\ rpm/div$**; Channels 1 and 3:** $6.66\ A/div$**).**

Figure 11 highlights the transient response during Event A, showing that the speed loop presents adequate damping and stable dynamic behavior, consistent with the selected phase margin and crossover frequency adopted during the frequency-domain controller design.

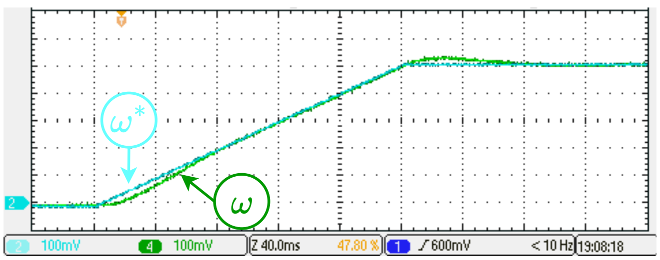

FIGURE 11. Detailed view of the rotor speed transient response during the acceleration event (Event A) (Channels 2 and 4: $200\ rpm/div$**).**

Figure 12 presents the phase-current waveforms obtained after Event E of the driving routine. In addition, the harmonic spectrum of the phase currents is summarized in Table 5. As observed, the phase currents present balanced sinusoidal waveforms with low Total Harmonic Distortion (THD) is 2.4%. The harmonic content presented in Table 5 confirms the low distortion characteristics of the drive system. The dominant low-order components, particularly the $5th$- and $7th$-order harmonics, remain at reduced levels for all phase currents.

TABLE 5. Harmonic content relative to fundamental (in $\%$**) of phase currents of** $11\ A$ **in steady state after Event E.**

Harmonic order	I_a	I_b	I_c	I_x	I_y	I_z
5th	0.27	0.41	0.14	0.37	0.44	0.17
7th	0.27	0.42	0.16	0.22	0.45	0.25
11th	0.17	0.20	0.04	0.15	0.20	0.24
13th	0.11	0.15	0.12	0.08	0.17	0.10
17th	0.02	0.06	0.06	0.03	0.13	0.16
19th	0.08	0.08	0.08	0.08	0.12	0.15

The results demonstrate that the proposed control method, incorporating derivative-free decoupling, enables the application of a SISO design approach, as the effects of cross-coupling are effectively mitigated. Consequently, the system dynamics closely match the designed current and speed control loop specifications. Furthermore, the proposed strategy does not degrade the current waveform quality.

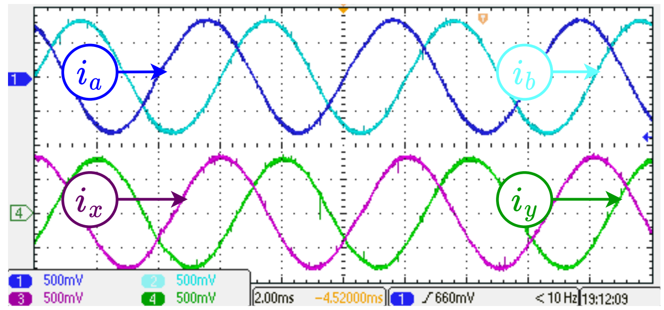

FIGURE 12. Steady-state six-phase current waveforms after the application of the load disturbance (Event E) ($6.66\ A/div$ **for all channels).**

D. DC-Link Voltage Ripple Influence

To further assess the proposed control strategy under practical operating conditions, the ideal DC voltage source is replaced by a three-phase diode rectifier supplying the DC-link. The average DC-link voltage level considered for this test is approximately $100\ V$. Consequently, the DC-link voltage exhibits the characteristic ripple commonly found in industrial drive systems. A capacitor bank equal to $1\ mF$ is considered in the DC-side of each VSI.

Figure 13 presents the DC-link voltage together with the corresponding motor currents. Although the DC-link voltage contains a noticeable low-frequency ripple, the proposed controller maintains satisfactory current regulation. Moreover, the THD remains below 2.5%, indicating that the current quality is only slightly affected compared with the result presented in Figure 12. This result further demonstrates the effectiveness of the proposed derivative-free decoupling strategy under these supply conditions.

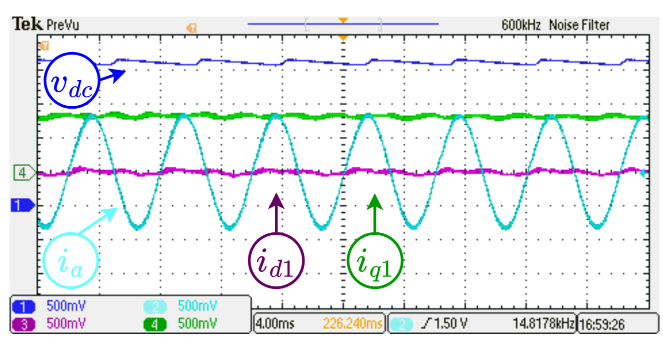

FIGURE 13. Steady-state responses during Event E with a three-phase diode rectifier supplying the DC link. (Channel 1: $25\ V/div$**; Channels 2, 3 and 4:** $6.66\ A/div$**.**

E. Influence of Parameter Mismatch

To verify the system behavior under parameter uncertainties, an additional test is carried out considering simultaneous variations in the stator resistance, stator inductance, and permanent magnet flux linkage with respect to their nominal values. The stator inductance and permanent magnet flux linkage are increased by 40%, while the stator resistance is reduced by 40% from their nominal values. This scenario emulates a practical mismatch between the machine parameters used for controller design and the actual machine. Figure 14 depicts the system behavior with parameter mismatch under step change of the current reference. Since the controller gains are computed from the nominal machine parameters, these variations avoid the exact cancellation between the controller zero and the plant slow pole. Consequently, the inner closed-loop system no longer exhibits the desired first-order behavior, resulting in the expected second-order transient response with 17 $\%$ overshoot and 10 ms of settling time. Nevertheless, the proposed control strategy preserves stable operation and satisfactory dynamic performance under these parameter variations.

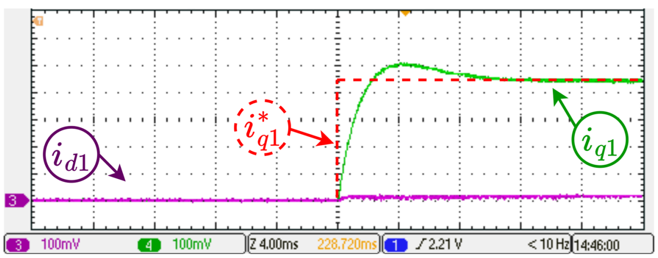

FIGURE 14. Current response under a $6\ A$ q-axis current step with parameters mismatch ($1.33\ A/div$ for all channels).

It is worth noting that the controller tuning method adopted in this work is intentionally selected because it provides a first-order closed-loop response under nominal conditions, making deviations caused by parameter uncertainties readily observable. Other controller design approaches could also be employed without affecting the applicability of the proposed decoupling method.

F. Remarks on Practical Implementation

The proposed control strategy is verified using a HIL platform, where the control algorithm is executed on a DSP while the electrical machine is emulated in real time. Consequently, practical implementation aspects such as digital control delays, finite sampling frequency, PWM operation, and signal quantization are naturally considered during the validation process.

Among the practical nonidealities encountered in electric drive systems, measurement noise deserves particular attention, since derivative operations are well known to amplify high-frequency components, including switching ripple and sensor noise. Because the proposed decoupling strategy does not require current derivative calculations, it is inherently less sensitive to these effects than the conventional derivative-based implementation. This characteristic is evidenced by the HIL results presented in Figure 8, where the proposed method achieves a significantly smoother current response while maintaining the desired dynamic performance. A comprehensive robustness assessment considering parameter uncertainties, manufacturing tolerances, and mechanical asymmetries is beyond the scope of this work. Nevertheless, the proposed strategy is expected to provide improved implementation by avoiding derivative-based computations.

VI. CONCLUSIONS

This paper presented the modeling, control design, and HIL evaluation of an asymmetric 6ϕ-PMSM supplied by dual three-phase VSIs. A state-space modeling of the machine is developed, allowing the investigation and comparative analysis of two different decoupling strategies for current control applications.

Based on the developed model, a cascaded control architecture composed of parallel inner current loops and an outer speed loop is designed. In addition, a frequency-domain tuning methodology based solely on the selection of the current-loop time constant and the desired phase margin is adopted, allowing all controller gains to be analytically determined. The proposed control structure achieves fast transient response, satisfactory disturbance rejection capability, stable speed regulation, and low harmonic distortion under different operating conditions. Furthermore, the current dynamics closely matched the designed first-order response, validating both the developed model and the adopted controller tuning methodology. The speed response also matched the designed control specifications.

The obtained results demonstrated that the proposed derivative-free decoupling strategy effectively mitigates the coupling effects between coordinates and subsystems while avoiding the derivative operations required by conventional approaches. Consequently, the proposed method significantly reduced sensitivity to switching ripple, quantization effects, and measurement noise under real-time DSP implementation.

Although the obtained results demonstrate the effectiveness of the proposed strategy under real-time Hardware-in-the-Loop conditions, the validation presented in this work is limited to the HIL platform. Therefore, experimental validation using a physical asymmetric six-phase PMSM prototype should be addressed in future work to further assess the proposed control strategy under practical operating conditions.

ACKNOWLEDGMENT

This work was carried out with the support of the Graduate Program in Electrical Engineering of the Universidade Federal de Minas Gerais (PPGEE-UFMG), the Coordination for the Improvement of Higher Education Personnel – Brazil (CAPES) – Financing Code 001, through the Academic

Excellence Program (PROEX), and the Fundação de Amparo à Pesquisa do Estado de Minas Gerais (FAPEMIG), under Grant No. APQ-02359-21.

AUTHOR'S CONTRIBUTIONS

L.D.GIOVANNINI: Conceptualization, Formal Analysis, Investigation, Methodology, Resources, Validation, Writing – Original Draft, Writing – Review & Editing. **A.C.B.DIAS:** Conceptualization, Formal Analysis, Investigation, Methodology, Resources, Validation, Writing – Original Draft, Writing – Review & Editing. **L.M.F.MORAIS:** Conceptualization, Formal Analysis, Investigation, Methodology, Resources, Validation, Writing – Original Draft, Writing – Review & Editing. **G.A.FOGLI:** Conceptualization, Formal Analysis, Investigation, Methodology, Resources, Validation, Writing – Original Draft, Writing – Review & Editing.

PLAGIARISM POLICY

This article was submitted to the similarity system provided by Crossref and powered by iThenticate – Similarity Check.

DATA AVAILABILITY

The data used in this research is available in the body of the document.

REFERENCES

[1] N. Novas, R. M. Garcia Salvador, F. Portillo, I. Robalo, A. Alcayde, M. Fernández-Ros, J. A. Gázquez, "Global Perspectives on and Research Challenges for Electric Vehicles", *Vehicles*, vol. 4, no. 4, pp. 1246–1276, 2022, doi:10.3390/vehicles4040066.

[2] V. H. K. Ries, G. Waltrich, A. Vaccari, "Estimativa de Mapa de Eficiência para Máquinas Elétricas Através do Método de Filtro de Kalman Estendido", *Eletrônica de Potência*, vol. 29, pp. e202426–e202426, 2024, doi:10.18618/REP.2005.2.061068.

[3] J. B. V. Neto, V. H. K. Ries, G. Waltrich, "Controle de velocidade de uma máquina de ímãs permanentes tolerante a falhas em conjunto com técnica de máximo torque por ampere", *Eletrônica de Potência*, vol. 29, pp. e202434–e202434, 2024, doi:10.18618/REP.e202434.

[4] Q. Wang, S. Wang, C. Chen, "Review of sensorless control techniques for PMSM drives", *IEEJ Transactions on Electrical and Electronic Engineering*, vol. 14, no. 10, pp. 1543–1552, 2019, doi:10.1002/tee.22974.

[5] M. Furmanik, L. Gorel, D. Konvičný, P. Rafajdus, "Comparative Study and Overview of Field-Oriented Control Techniques for Six-Phase PMSMs", *Applied Sciences*, vol. 11, no. 17, 2021, doi:10.3390/app11177841.

[6] J. Shen, X. Wang, Z. Zhang, S. Ren, D. Ma, D. Xiao, "Research on the Application of Dual Three-Phase PMSM in Renewable Energy System", *in 2023 26th International Conference on Electrical Machines and Systems (ICEMS)*, pp. 3475–3479, 2023, doi:10.1109/ICEMS59686.2023.10344728.

[7] S. Bharti, C. Bhende, O. Ray, "Control of Six-Phase Permanent Magnet Synchronous Motor for Electric Vehicle Application", *in 2022 IEEE 2nd International Conference on Sustainable Energy and Future Electric Transportation (SeFeT)*, pp. 1–6, 2022, doi:10.1109/SeFeT55524.2022.9908704.

[8] H. Gao, Z. Zhang, Y. Liu, W. Huang, H. Xue, "Development and Analysis of Dual Three-Phase PMSM With Phase-Shifted Hybrid Winding for Aircraft Electric Propulsion Application", *IEEE Transactions on Transportation Electrification*, vol. 10, no. 3, pp. 6497–6508, 2024, doi:10.1109/TTE.2023.3334026.

[9] S. Hu, Z. Liang, W. Zhang, X. He, "Research on the Integration of Hybrid Energy Storage System and Dual Three-Phase PMSM Drive in EV", *IEEE Transactions on Industrial Electronics*, vol. 65, no. 8, pp. 6602–6611, 2018, doi:10.1109/TIE.2017.2752141.

[10] Y. Hu, Z. Q. Zhu, M. Odavic, "Comparison of Two-Individual Current Control and Vector Space Decomposition Control for Dual Three-Phase PMSM", *IEEE Transactions on Industry Applications*, vol. 53, no. 5, pp. 4483–4492, 2017, doi:10.1109/TIA.2017.2703682.

[11] Y. Hu, Z.-Q. Zhu, K. Liu, "Current Control for Dual Three-Phase Permanent Magnet Synchronous Motors Accounting for Current Unbalance and Harmonics", *IEEE Journal of Emerging and Selected Topics in Power Electronics*, vol. 2, no. 2, pp. 272–284, 2014, doi:10.1109/JESTPE.2014.2299240.

[12] L. D. Giovannini, A. de Carvalho Batista Dias, L. M. F. Morais, G. A. Fogli, "Modeling and Control of a Six-Phase PMSM Using Two Three-Phase Inverters with Decoupling Influence Analysis", *in 2025 Brazilian Power Electronics Conference (COBEP)*, pp. 1–6, 2025, doi:10.1109/COBEP66423.2025.11231710.

[13] Y. Luo, K. Yang, Y. Zheng, "Luenberger Observer-Based Model Predictive Control for Six-Phase PMSM Motor With Localization Error Compensation", *IEEE Transactions on Industrial Electronics*, vol. 70, no. 11, pp. 10800–10810, 2023, doi:10.1109/TIE.2022.3229340.

[14] Z. Song, C. Liu, Z. Dong, R. Huang, "Improved Multi-Stage Decoupling Space Vector Modulation for Asymmetrical Multi-Phase PMSM With Series Winding Connection", *IEEE Transactions on Power Electronics*, vol. 37, no. 9, pp. 10951–10966, 2022, doi:10.1109/TPEL.2022.3163275.

[15] Y. He, Y. Wang, J. Wu, Y. Feng, J. Liu, "A simple current sharing scheme for dual three-phase permanent-magnet synchronous motor drives", *in 2010 Twenty-Fifth Annual IEEE Applied Power Electronics Conference and Exposition (APEC)*, pp. 1093–1096, 2010, doi:10.1109/APEC.2010.5433366.

[16] Y. Luo, X. Zhang, S. Niu, "A Hybrid Two-Stage Control Solution for Six-Phase PMSM Motor With Improved Performance", *IEEE Journal of Emerging and Selected Topics in Power Electronics*, vol. 10, no. 5, pp. 5435–5445, 2022, doi:10.1109/JESTPE.2022.3141487.

[17] H. Yan, L. Liu, B. Ge, "Decoupling control of asymmetric Six-Phase PMSM two-motor series-connected system with harmonic compensation", *Journal of Physics: Conference Series*, vol. 3043, no. 1, p. 012130, jun 2025, doi:10.1088/1742-6596/3043/1/012130.

[18] A. de Carvalho Batista Dias, L. D. Giovannini, G. M. Auler, G. A. Fogli, "Analysis and Design of State Observers Applied to a Six-Phase Permanent Magnet Synchronous Machine", *in 2025 Brazilian Power Electronics Conference (COBEP)*, pp. 01–07, 2025, doi:10.1109/COBEP66423.2025.11231507.

[19] J. Karttunen, S. Kallio, P. Peltoniemi, P. Silventoinen, O. Pyrhonen, "Dual three-phase permanent magnet synchronous machine supplied by two independent voltage source inverters", pp. 741–747, 06 2012, doi:10.1109/SPEEDAM.2012.6264448.

[20] J. Karttunen, S. Kallio, P. Peltoniemi, P. Silventoinen, "Current Harmonic Compensation in Dual Three-Phase PMSMs Using a Disturbance Observer", *IEEE Transactions on Industrial Electronics*, vol. 63, no. 1, pp. 583–594, 2016, doi:10.1109/TIE.2015.2461519.

[21] Y. Zhao, T. Lipo, "Space vector PWM control of dual three-phase induction machine using vector space decomposition", *IEEE Transactions on Industry Applications*, vol. 31, no. 5, pp. 1100–1109, 1995, doi:10.1109/28.464525.

[22] J. Karttunen, S. Kallio, P. Peltoniemi, P. Silventoinen, O. Pyrhönen, "Decoupled Vector Control Scheme for Dual Three-Phase Permanent Magnet Synchronous Machines", *IEEE Transactions on Industrial Electronics*, vol. 61, no. 5, pp. 2185–2196, 2014, doi:10.1109/TIE.2013.2270219.

[23] S.-K. Sul, *Control of electric machine drive systems*, John Wiley & Sons, 2011, doi:10.1002/9780470876541.

[24] G. A. Fogli, I. D. Souza, M. C. Fernandes, P. M. Almeida, P. G. Barbosa, "Dispatchable distributed generation using a back-to-back converter for grid-forming improvements based on feed-forward action with load current prediction", *IET Power Electronics*, vol. 13, no. 16, pp. 3686–3696, 2020, doi:10.1049/iet-pel.2020.0215.

[25] M. Furmanik, P. Makys, P. Rafajdus, "Self-Sensing Six-Phase PMSM Drive Based on Back-EMF Measurement", *Applied Sciences*, vol. 13, no. 2, 2023, doi:10.3390/app13021077.

BIOGRAPHIES

Letícia D. Giovannini Letícia D. Giovannini received the B.S degree in Electrical Engineering from Universidade Federal de Minas Gerais (UFMG), Brazil, in 2025, and has been pursuing the M.Sc. degree in Electronic Engineering at Instituto Tecnológico da Aeronáutica (ITA), Brazil, since 2025. Her research interests include modeling and control of power electronic converters.

Arthur de C. B. Dias received the B.S. degree in control and automation engineering from Universidade Federal de Minas Gerais (UFMG), Brazil, in 2023, and is an graduate student in electrical engineering at UFMG, since 2024. His research interests include modeling and control of electronic converters applied to electrical drives.

Lenin M. F. Morais received the bachelor's degree, the master's degree, and the doctor's degree, all in electrical engineering from the Federal University of Minas Gerais, Belo Horizonte, Brazil, in 2000, 2002, and 2007, respectively. He is currently a Full Professor with the Electronics Engineering Department, Federal University of Minas Gerais. He was a Postdoctoral Intern with the Laboratoire Plasma et Conversion d'Energie - LAPLACE, Université Toulouse III Paul Sabatier, Toulouse, France, and with the Institut de Recherche Technologique - IRT Saint Exupéry, Toulouse, France. IEEE Senior Member and member of the IEEE Power Electronics Society, and Member of SOBRAEP (Brazilian Power Electronics Society) since 2005. He has experience in the field of electrical engineering, with emphasis on power electronics, industrial electronics, and electronic systems and controls. His research interests mainly include the following: projects of converters with high density of power/high performance, electronic reactors for high intensity discharge lamps, power LEDs, circuits for power factor correction, repetitive control, control based on passivity, PWM methods.

Gabriel A. Fogli received the B.S. degree in electronics and telecommunication engineering from Pontifícia Universidade Católica de Minas Gerais (PUC Minas), Brazil, in 2011, and the M.Sc. and Ph.D. degrees in electrical engineering from the Universidade Federal de Juiz de Fora (UFJF), Brazil, in 2014 and 2018, respectively. He was a Professor with the Department of Electrical Engineering, Universidade Federal de Ouro Preto (UFOP), Brazil, from 2016 to 2019. Since 2019, he has been a Professor with the Universidade Federal de Minas Gerais (UFMG), Brazil. He is a member of the Brazilian Power Electronics Society (SOBRAEP) and the IEEE Power Electronics Society (PELS). His research interests include modeling and control of power electronic converters and distributed generation applications.